Title

Multi-scale microstructural investigation of a laser 3D printed Ni-based superalloy

Authors

Li, Yao

Chen, Kai

Narayan, R Lakshmi

et al.

Publication Date

2020-08-01

DOI

10.1016/j.addma.2020.101220

Peer reviewed

Multi-scale microstructural investigation of a laser 3D printed Ni-based superalloy

Yao Li[1,2], Kai Chen[2*], R. Lakshmi Narayan[3], Upadrasta Ramamurty[4], Yudong Wang[1], Juncheng Long[1], Nobumichi Tamura[5], Xin Zhou[6]

1. *School of Materials Science and Engineering, Chang'an University, Xi'an, Shaanxi 710064, China*
2. *Center for Advancing Materials Performance from the Nanoscale (CAMP-Nano), State Key Laboratory for Mechanical Behavior of Materials, Xi'an Jiaotong University, Xi'an, Shaanxi 710049, China*
3. *Department of Materials Science and Engineering, Indian Institute of Technology, Delhi, New Delhi 110016, India*
4. *School of Mechanical and Aerospace Engineering, Nanyang Technological University, Singapore 639798, Singapore*
5. *Advanced Light Source, Lawrence Berkeley National Laboratory, Berkeley, California 94720, USA*
6. *Science and Technology on Plasma Dynamics Laboratory, Air Force Engineering University, Xi'an 710038, China*

* Author to whom correspondence should be addressed. Email: kchenlbl@gmail.com (K.C.)

The hierarchical microstructure of a laser 3D printed Ni-based superalloy was examined at multiple length scales. The sub-millimeter-sized columnar crystal grains are composed of micron-sized cellular colonies. The crystal grains grow in epitaxy with the substrate under the large thermal gradient and high cooling rate. The cell boundaries, decorated with γ/γ′ eutectics, μ-phase precipitates and high density of dislocations, show enrichment of γ′ forming elements and low-angle misorientations. Dislocations trapped in the intra-cellular regions are characterized as statistically stored dislocations with no detectable contribution to lattice curvature, and are the results of the interaction between dislocations and γ′ precipitates.

Keywords: directed energy deposition; hierarchical microstructures; cellular structures; non-uniform dislocation distribution; Ni-based superalloys

1. Introduction

Laser additive manufacturing, which is commonly referred to as laser 3D printing (L3DP), has great potential for near net shape manufacturing as well as repair of gas turbine engine components composed of single crystal or directionally solidified Ni-based superalloys with high γ′ content (> 60%) [1]. Based on the power feeding strategy, L3DP can be categorized into either direct energy deposition (DED) orpowder bed fusion (PBF). Due to the focused heat source and reduced heat input, a steep temperature gradient, parallel to the building direction, is present during both the DED and PBF processes, facilitating epitaxial crystal growth with the base plate metal orientation. Simultaneously, heterogeneous microstructures with length scales ranging from nanometer to sub-millimeter are generated from the rapid solidification of the DED and LPBF process [2–5]. These are otherwise not feasible through conventional methods of manufacturing. The high cooling rates inherent to L3DP severely suppress the growth of secondary dendrite arms, making it challenging to distinguish between cells and dendrites [6] in the absence of crystal orientation knowledge. Hence, the term "cell" is generally used to denote the cellular/dendritic structures in 3D printed alloys. The fine cellular structures, accompanied by both elemental and dislocation partitioning, have been reported in a variety of 3D printed face-centered cubic alloys, including Al alloys [7], austenite stainless steels [2,8,9], high-entropy alloys [10] and Ni-based superalloys [11–14].

The simultaneous enhancements in strength and ductility of 3D printed alloys, compared to their conventionally manufactured counterparts, are attributed to such cellular structures [2,8]. There is however no consensus on the exact mechanism leading to the observed strengthening. In the absence of detailed characterization of the

misorientations across them, the cell boundaries are treated as conventional high-angle grain boundaries (HAGBs), leading to a Hall-Petch relation based description of strength [2]. Some authors however argue that cell boundaries cannot be regarded as HAGBs, and attribute the observed strengthening to dislocation interactions (work hardening) together with elemental segregation (solid solution strengthening) and crystal grain refinement (if any) [10,15]. In this context, it is worth noting that most of such observations/discussions are based on austenite stainless steels, high entropy alloys and Ni-based superalloys with low γ′ content (e.g. IN718 and IN625) [13,16]. However, only a few studies have been reported in laser 3D printed directionally solidified and single crystalline Ni-based superalloys with high Ti/Al contents and thus high γ′ fraction, especially without post processing heat treatment [11,17]. In particular, detailed knowledge of the dislocation type and distribution, and how the chemical inhomogeneity associated with the cellular structure influences the size, morphology, and phase of the strengthening precipitates is essential to understand the mechanical performance of 3D printed Ni-based superalloys. Keeping this in view, we report here the results of a comprehensive microstructural study on a Ni-based superalloy manufactured by DED technique.

2. Materials and methods

Gas atomized DD4 superalloy powders with a diameter range of 40 to 120 μm were used as the feedstock for the DED process. An in-house developed co-axial laser cladding apparatus was employed and a 7 mm diameter 15 mm long cylinder was deposited on the (001) surface of a directionally solidified Ni-based superalloy DZ125L substrate using a scan protocol where the scanning direction of each layer was perpendicular to the previous one. The nominal compositions of DD4 powders and

DZ125L substrate are listed in Table 1. The DED process was carried out with a fixed laser power of 230 W and a scan rate of 10 mm/s under an Ar protective atmosphere. Powders carried by Ar gas were injected into the melt pool at a rate of ~9 mm^3/s. More detailed information about the manufacturing process can be found elsewhere [18].

Table 1. Nominal compositions of the substrate and powders.

Composition (wt%)	C	Cr	Co	Mo	W	Al	Ti	Ta	Ni
DZ125L substrate	0.12	8.74	9.54	2.21	6.46	5.03	3.18	3.96	Balance
DD4 powders	0.004	8.97	7.26	1.94	6.91	3.94	4.22	3.73	Balance

After the DED process, the specimens were cut from the cylinders. After mechanical polishing and electrical etching in an aqueous solution consisting of 30 vol % H_3PO_4, microstructural investigation was carried out under an optical microscope (OM, Carl Zeiss Axio Scope A1) and a scanning electron microscope (SEM, Hitachi SU6600) equipped with energy dispersive spectroscopy (EDS). Electron backscattered diffraction (EBSD) equipped in a focused ion beam system (FIB, FEI Helios 600 NanoLab DualBeam) was conducted for the study of grain structures. An EBSD measurement from the cross-sectional area up to 1350 × 1150 μm^2 was acquired with 5 μm step size and post-processed by MTEX toolbox [19]. Synchrotron X-ray microdiffraction (μXRD) was conducted on beamline 12.3.2 at the Advanced Light Source of the Lawrence Berkeley National Laboratory. The cross-sectional specimen was mounted on the sample stage at a 45° incline angle relative to the polychromatic X-ray beam (5 ~ 24 keV). 3600 Laue Patterns (LP) were collected using a two-dimensional X-ray detector (DECTRIS Pilatus 1M) over an area of 60 × 60 μm^2 with 1 μm step size and 0.5 s exposure time at each scan position, and subsequently indexed by using the custom-developed software package XMAS for mapping the orientation deviations. Full details of the μXRD setup and LP indexing process can be found in Ref.

[20,21]. The EBSD and μXRD specimens were fabricated by electrical polishing in a solution of 92% alcohol and 8% perchloric acid at 25 V. In addition, the cross-sectional specimen was ground, thinned with a twin-jet electro-polishing machine, and investigated under transmission electron microscope (TEM, 200kV JOEL 2100F) to examine the microstructures at the nano-scale.

3. Results

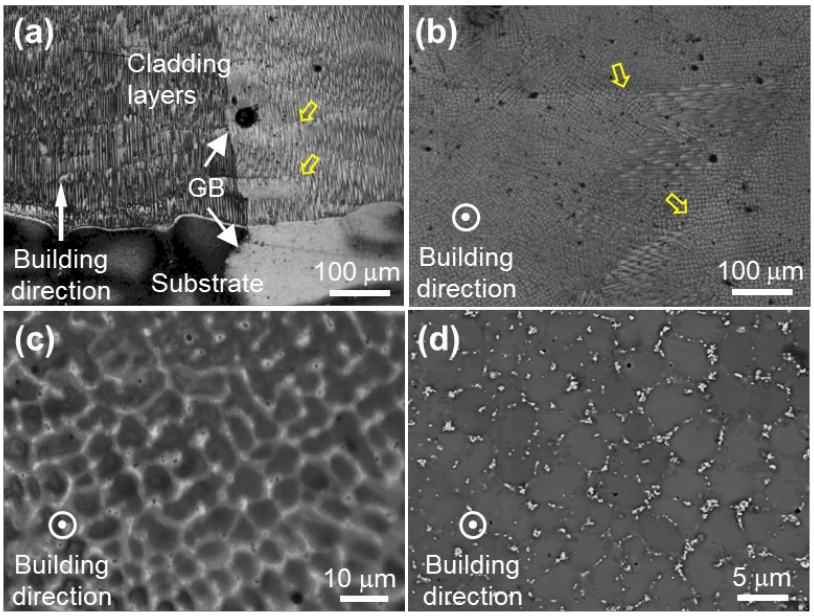

Figure 1. The cellular microstructures in the DEDed superalloy. OM images collected from the (a) longitudinal section and (b) cross sectional specimens, respectively. The yellow arrows in (a) and (b) denote the fusion lines. (c) An enlarged view of (b) showing the typical cell morphology. (d) BSE SEM image showing the dispersed precipitates along the cell boundaries from the cross-sectional view.

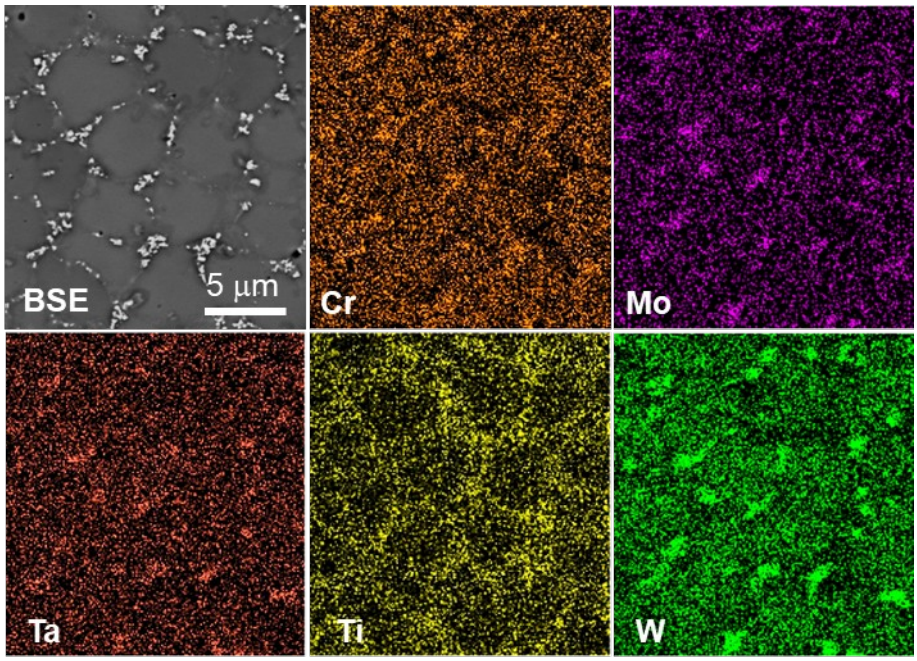

Figure 2. EDS element distributions collected from the cross-sectional specimen.

Low magnification optical micrograph (Fig. 1a) of the longitudinal section of the specimen, shows the substrate/cladding layer interface and the layer-by-layer deposition patterns outlined by the fusion lines, which are also visible from the cross-sectional view in Fig. 1b. The thickness of each deposited layer was measured to be about 100 μm. The observation of grain boundaries (GBs), one of which is marked with white arrows in Fig. 1a, running across multiple deposited layers from substrate, implies epitaxial growth of the columnar grains. In each grain, columnar cells orient preferentially parallel to the building direction. From the cross-sectional view in Fig. 1c, these cell colonies appear equiaxed in the direction transverse to the building direction. The cells can therefore be viewed as long cylindrical rods with an average diameter of ~6 μm. Under the backscattered electron (BSE) mode of SEM, the cells are outlined by the high density of nano-sized particles with bright contrast at the boundaries (Fig. 1d). These regions are enriched in Cr, Mo, Ta, Ti and W, as revealed in the energy dispersive spectroscopy (EDS) maps (Fig. 2).

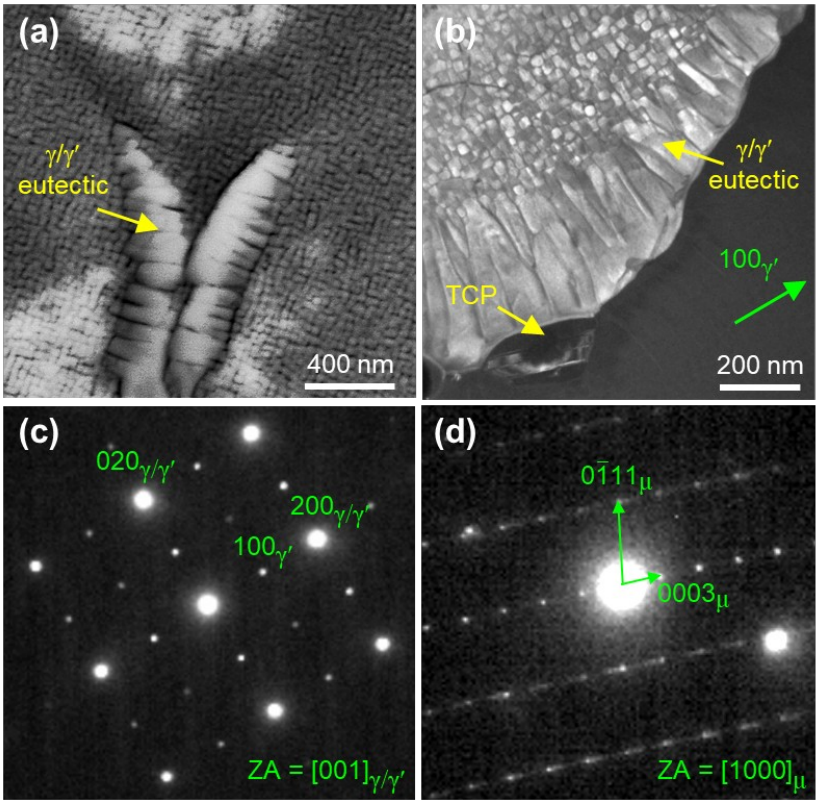

Figure 3. The phase distribution in the DEDed superalloy. The combination of (a) BSE SEM and (b) TEM dark field images reveals two types of ɣ′ morphologies. SEAD patterns evidence (c) the coherent ɣ/ɣ′ microstructure and (d) the μ-phase precipitates.

From the SEM image (Fig. 3a) and dark field TEM image (Fig. 3b) illuminated by the 100 reflection of ɣ′ precipitates (Fig. 3c), two different morphologies of ɣ′ precipitates are observed. In the intra-cellular regions, small, close-packed and neatly ordered near-cuboidal ɣ′ precipitates with an average size of ~30 nm can be seen. Along the cell boundaries, however, rectangular ɣ/ɣ′ eutectic phases, with a typical ɣ′ size of ~80 nm (width) × 200 nm (length), aggregate in a comb-like morphology. Moreover, a topologically closed-packed (TCP) particle near the ɣ/ɣ′ eutectic was identified as the μ-phase with rhombohedral crystal structure, as evidenced from the corresponding selected area electron diffraction (SAED) study in Fig. 3d.

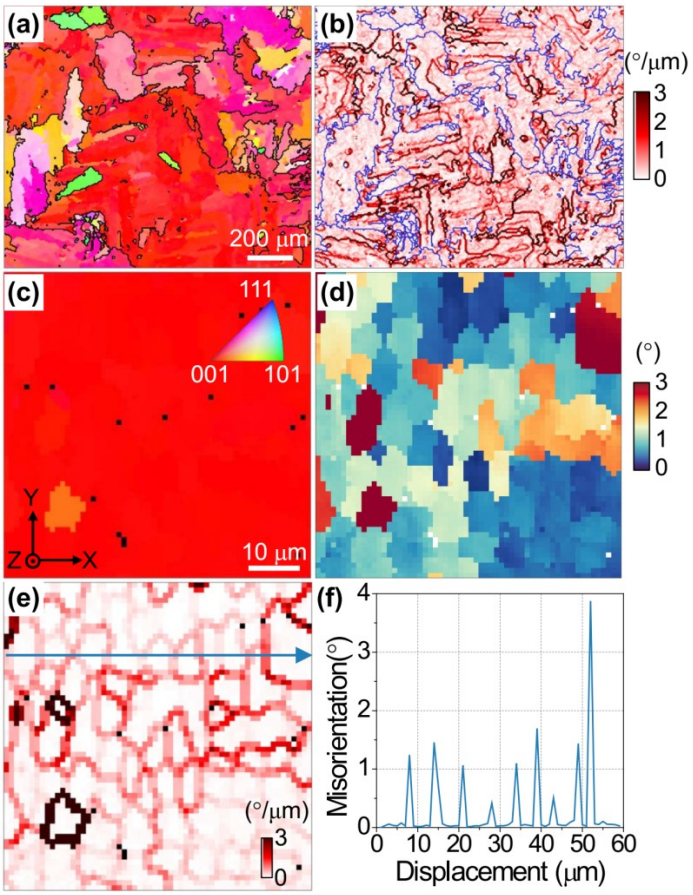

Figure 4. Crystal orientation and misorientation analysis of cross-sectional specimen. (a) IPF-Z and (b) KAM maps of an EBSD measurement. The black and blue lines in (a) and (b) delineate the GBs with misorientation angles larger than 15°, respectively. (c) IPF-Z, (d) misorientation angle and (e) KAM maps of the μXRD scan. (f) A linear profile of point-to-point misorientation along the horizontal arrow in (e).

From the out-of-plane inverse pole figure (IPF-Z) map obtained using EBSD in Fig. 4a, a broad grain size distribution is observed and the largest grain is close to 1 mm in diameter. Most of the grains in red reveal that their [001] directions are almost parallel to the building direction. Since the aim of the present study is to surrogate the repair of a turbine blade tip, the substrate surface normal is also along the [001] direction. Thus the deposited layers are epitaxial with the substrate. The uneven colors in the grain interior indicate the presence of intragranular orientation gradients, and the low angle grain boundaries (LAGBs) visible in the kernel average misorientation (KAM) map (Fig. 4b) confirm the existence of a sub-grain structure. It should be noted

that the value of the extent of orientation variance between cellular colonies is barely accessible by conventional EBSD method [2] due to its poor angular resolution (~0.5°). Therefore, synchrotron μXRD technique with superior orientation resolution (< 0.01°) was employed [22].

As seen in the IPF-Z map of the synchrotron μXRD study (Fig. 4c), the whole scanned area has a similar orientation, yet an isolated sub-grain domain, in orange, deviates ~12° relatively to its surroundings. Since the sub-grain orientation variation is hardly discernable from the IPF-Z map, the misorientation angle of each scan spot relative to the average orientation of the whole scan is calculated and shown in Fig. 4d. The map shows the whole scan area is composed of a multitude of cellular colonies with distinctive colors. This suggests that the growth direction of each cell is slightly misaligned, while the orientation within each single cell is nearly identical. Consequently, LAGBs observed from the KAM map (Fig. 4e) delineate the cell boundaries and hence outline the size/shape of cell colonies, in agreement with the optical microscopy and SEM images displayed in Figs. 1b and 1c. As seen in Fig. 4f, ten cells can be clearly distinguished from the nine peaks along the misorientation profile obtained through the blue horizontal line in Fig. 4e. The misorientation angle between each pair of adjacent cells ranges from 1° to 4°, while the low amplitude orientation variations (< 0.1°) in the intra-cellular scale are negligible.

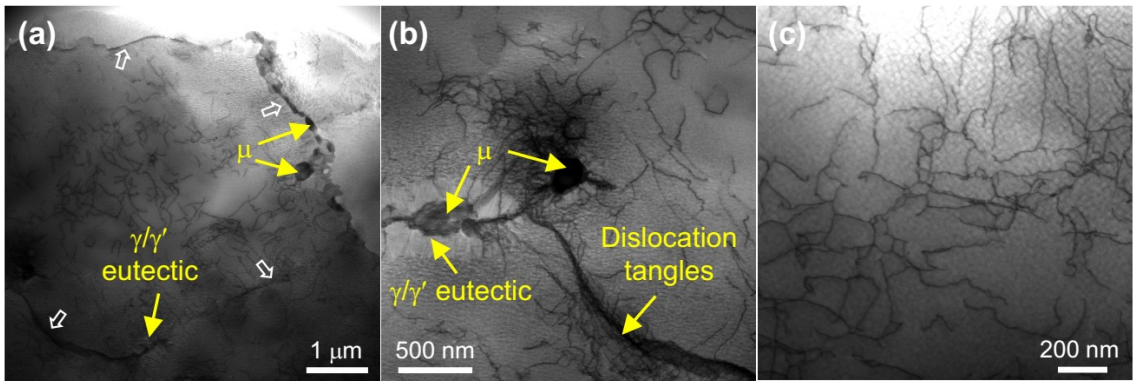

Figure 5. STEM TEM analysis of dislocation configurations at the cellular scale. (a) A full view of a cell colony and dislocation configurations, (b) near the cell boundary, and (c) in the cell interior.

In general, LAGBs are formed as dislocations arrange into energetically favorable configurations and are necessary for the accommodation of lattice curvatures [23]. To verify this, we examined the dislocation structure in the cross-sectional specimen using TEM in scanning transmission electron microscopy (STEM) mode. As seen in Fig. 5a, the cell boundaries, in dark contrast and denoted by hollow arrows, are decorated with γ/γ′ eutectics and irregular shaped μ particles with average size of about 200 nm. An enlarged view displayed in Fig. 5b suggests large populations of dislocations tangled along the cell boundary. Since these dislocations are not homogeneously distributed, possibly because their mobility is impeded by μ particles, LAGBs, and coarse γ′ precipitates of γ/γ′ eutectics, it is difficult to estimate their density quantitatively. In the interior of the cells, however, the dislocation lines are distributed more homogeneously (Fig. 5c). Using the line-intercept method adopted by Norfleet et al. [24], the dislocation density in the cell interior is estimated to be ~1.4 $\times 10^{14}$ m^{-2}.

4. Discussion

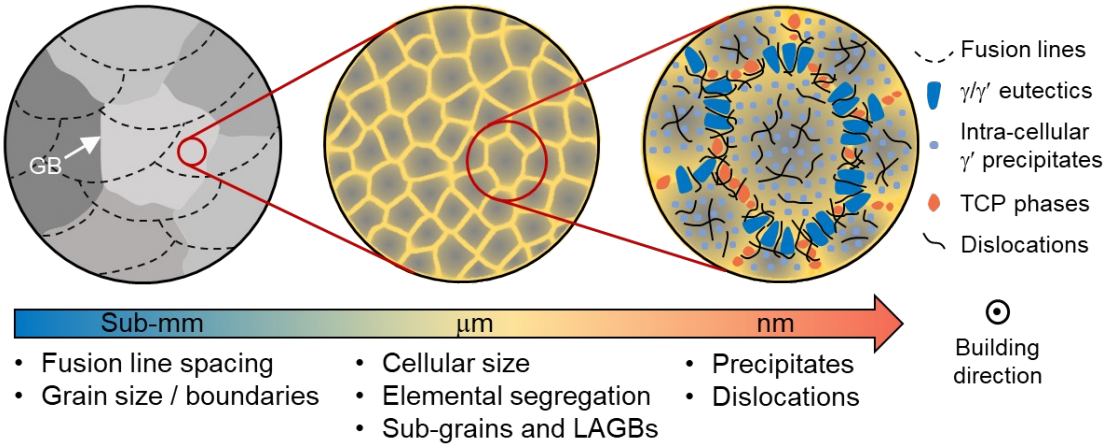

Figure 6. Schematic illustration of the microstructures from the sub-millimeter to nanometer scales in the cross-sectional view of DEDed Ni-based superalloy.

From the multi-scale characterization approach described above, the heterogeneous microstructure of the 3D printed superalloy, schematically displayed in Fig. 6, can be constructed. Although the crystal grains obtained in 3D printed superalloys are usually coarse (grain size of up to hundreds of microns or even at a centimeter scale for a single crystal [25]), they are composed of submicron to micron sized cellular structures, exhibiting elemental segregation, inhomogeneous distributions of dislocations and precipitates, and small misorientation between adjacent cells. The cell boundaries are enriched in γ′ forming elements, resulting in larger γ′ precipitates in the inter-cellular regions than in the cell interiors [26]. In some of the superalloys like the one studied here, particles with TCP phases are detected [27]. High and non-uniform density of tangled dislocations are observed along the cell boundaries. Dislocations also exist in the cell interior; although their density is lower than those along the cell boundaries, it is higher than those in the cell interiors of 3D printed stainless steels [2,8] and high entropy alloys [10]. Typically, the rapid cooling rate and the repeated heating/cooling cycles generated by the motion of the laser beam induce intense thermal stresses that can exceed the yield strength of the cladding materials [18]. Additionally, for γ′-strengthened Ni-based superalloy, the rapid precipitation of γ′ will also introduce pronounced phase transition stress due to the γ/γ′ misfit. The superimposition of thermal stresses and phase transition stresses induce a large number of dislocations both in the cell center and in the intercellular region. A possible reason for the distinguished intra-cellular dislocation distribution of superalloys studied here from the 3D printed stainless steels and high entropy alloys is the strong hindrance to dislocation mobility caused by the γ′ particles.

The cellular microstructure is due to the rapid solidification process during 3D

printing. According to the undercooling criterion [28], solidification microstructure depends on temperature gradient (G), solidification rate (R), and undercooling temperature (ΔT) of the melt pool. Cellular solidification prevails if $G/R > \Delta T/D$, where D is the diffusion coefficient. In L3DP, G usually reaches 10^5~10^7 K/s [29], which is at least 3 orders of magnitude higher than the cooling rate in traditional casting conditions. R is equal to $V\cos\theta$, where V is the laser scan speed and θ is the angle between laser scan direction and the solid-liquid interface of melt pool. As the multiplication of G and R, i.e. the cooling rate, is inversely proportional to the cell spacing (or primary dendrite arm spacing), the observed cell spacing (~6 μm) larger than most of other reported superalloys (~ 1 μm) fabricated by PBF [11,12] implies a relatively lower cooling rate in this study. Though the laser scan speed of LPBF is much larger than that of DED, the G values of different additive manufacturing methods are estimated to be in the same order of magnitude. As R is close to the laser scan speed, the resulting large G/R ratio of the present study is almost ~2 orders of magnitude larger than that of LPBF, facilitating the formation of cellular structures. It is also suggested that a high G gives rise to strong thermo-capillary convection due to the surface-tension driven instability, or Benard-Marangoni surface instability [30], which promotes the ejected γ′ forming elements to accumulate in the inter-cellular liquid, which, in turn, trigger the eutectic reaction L → γ + γ′ in the final stage of solidification [26,31]. Since the γ′ solvus rises with increasing content of γ′ forming elements, inter-cellular γ′ particles precipitate at a higher temperature and experience longer period over which they can coarsen [26]. Since superalloys with high W or/and Mo content show a strong tendency for μ-phase formation during conventional solidification, the μ-phase observed in this study is believed to nucleate directly from the inter-cellular liquid, i.e. primary μ-phase [32].

Moreover, as shown in Fig. S1 in the Supplementary Material, the lamellar features observed within the TCP particle imply the presence of growth faults, which may have been introduced by the thermal stress that arises during the 3D printing process [32].

As for the layer-by-layer deposition process, partial remelting of the underlying layers is necessary for a strong metallographic bond between two adjacent deposit layers. Simultaneously, the unmolten layers also serve as the substrate for the epitaxial growth of the newly formed cells. However, affected by the flowing field, cell growth deflects toward upper stream and the deflection angles varies at different locations in the melt pool [33], leading to a slight orientation variation between different cells. On the other hand, although the solidification cell growth front aligns along the favored [001] crystallographic direction, which is anti-parallel to the heat flux, the individual cells, regarded as cantilever beams, are anchored at the position of the solidus isotherm once the inter-cellular liquid starts to freeze and is subjected to bending moments and torques caused by thermal stresses [34]. Therefore, the accumulated misorientation is an outcome of the layer-by-layer building process. Because of the complex solidification process and the presence of plastic stresses, dislocations are also formed in the deformable γ channels and bow out between hard γ′ precipitates. In addition, the complex solidification paths, including melting, partial re-melting, cyclic annealing, γ′ dissolution and re-precipitation, lead to the inhomogeneous distribution of γ′ precipitates, resulting in complicated interactions between the dislocations and the γ′ precipitates. Thus the dislocations are distributed in the cells with random signs. [35]. In other words, these dislocations are statistically stored dislocations (SSDs). This is why the lattice curvature is not observed in the intra-cellular regions using the μXRD technique.

5. Conclusions

In summary, heterogeneous microstructures, including fusion lines, columnar grains, LAGBs as well as the elemental distribution, phase constituents and dislocation configurations at the cellular scale are investigated in a DEDed superalloy. The epitaxial growth of cells and columnar grains are attributed to the partial remelting of underlying deposit layers and the maximum heat flow antiparallel to the building direction. Cell boundaries, identified as LAGBs, are decorated with γ/γ′ eutectics, μ-phases and non-uniform dislocation arrangements, which are linked to the inter-cellular segregation of γ′ forming elements during the DED process. In contrast to the cell structures in other 3D printed alloys with small to negligible volume fraction of strengthening precipitates, intra-cellular dislocation density in the γ′-strengthened superalloys is significantly higher but do not contribute to lattice curvature, and is attributed to the interactions between dislocations and γ′ precipitates leading to the formation of SSDs.

Acknowledgements

We thank S.C. Lin and J. W. Kou for valuable discussions. Y. Li thanks Y. B. Qin and D. L. Zhang for TEM operation and data analysis. This work is supported by National Natural Science Foundation of China (Grant No. 51901026, 91860109, 51671154, 51927801) and the National Key Research and Development Program of China (Grant No. 2016YFB0700404). Y. L. acknowledges the support from the Fundamental Research Funds for the Central Universities (CHD No. 300102319301). The ALS is supported by the Director, Office of Science, Office of Basic Energy Sciences, Materials Science Division, of the U.S. Department of Energy under Contract No. DE-AC02-05CH11231 at LBNL.

References:

[1] R. Vilar, A. Almeida, Repair and manufacturing of single crystal Ni-based superalloys components by laser powder deposition—A review, J. Laser Appl. 27 (2015) S17004.

[2] Y.M. Wang, T. Voisin, J.T. McKeown, J. Ye, N.P. Calta, Z. Li, Z. Zeng, Y. Zhang, W. Chen, T.T. Roehling, R.T. Ott, M.K. Santala, P.J. Depond, M.J. Matthews, A. V. Hamza, T. Zhu, Additively manufactured hierarchical stainless steels with high strength and ductility, Nat. Mater. 17 (2018) 63–70.

[3] A. Basak, R. Acharya, S. Das, Epitaxial deposition of nickel-based superalloy René 142 through scanning laser epitaxy (SLE), Addit. Manuf. 22 (2018) 665–671.

[4] P. Kumar, O. Prakash, U. Ramamurty, Micro-and meso-structures and their influence on mechanical properties of selectively laser melted Ti-6Al-4V, Acta Mater. 154 (2018) 246–260.

[5] P. Kumar, U. Ramamurty, Microstructural optimization through heat treatment for enhancing the fracture toughness and fatigue crack growth resistance of selective laser melted Ti–6Al–4V alloy, Acta Mater. 169 (2019) 45–59.

[6] T.T. Roehling, S.S.Q. Wu, S.A. Khairallah, J.D. Roehling, S.S. Soezeri, M.F. Crumb, M.J. Matthews, Modulating laser intensity profile ellipticity for microstructural control during metal additive manufacturing, Acta Mater. 128 (2017) 197–206.

[7] B. Chen, S.K. Moon, X. Yao, G. Bi, J. Shen, J. Umeda, K. Kondoh, Strength and strain hardening of a selective laser melted AlSi10Mg alloy, Scr. Mater. 141 (2017) 45–49.

[8] L. Liu, Q. Ding, Y. Zhong, J. Zou, J. Wu, Y.L. Chiu, J. Li, Z. Zhang, Q. Yu, Z. Shen, Dislocation network in additive manufactured steel breaks strength–ductility trade-off, Mater. Today. 21 (2018) 354–361.

[9] J. Suryawanshi, K.G. Prashanth, U. Ramamurty, Tensile, fracture, and fatigue crack growth properties of a 3D printed maraging steel through selective laser melting, J. Alloys Compd. 725 (2017) 355–364.

[10] Z.G. Zhu, X.H. An, W.J. Lu, Z.M. Li, F.L. Ng, X.Z. Liao, U. Ramamurty, S.M.L. Nai, J. Wei, Selective laser melting enabling the hierarchically heterogeneous microstructure and excellent mechanical properties in an interstitial solute strengthened high entropy alloy, Mater. Res. Lett. 7 (2019) 453–459.

[11] X. Wang, L.N. Carter, B. Pang, M.M. Attallah, M.H. Loretto, Microstructure and yield strength of SLM-fabricated CM247LC Ni-Superalloy, Acta Mater. 128 (2017) 87–95.

[12] M. Ni, S. Liu, C. Chen, R. Li, X. Zhang, K. Zhou, Effect of heat treatment on the microstructural evolution of a precipitation-hardened superalloy produced by selective laser melting, Mater. Sci. Eng. A. 748 (2019) 275–285.

[13] M. Pröbstle, S. Neumeier, J. Hopfenmüller, L.P. Freund, T. Niendorf, D. Schwarze, M. Göken, Superior creep strength of a nickel-based superalloy produced by selective laser melting, Mater. Sci. Eng. A. 674 (2016) 299–307.

[14] S. Sui, J. Chen, R. Zhang, X. Ming, F. Liu, X. Lin, The tensile deformation behavior of laser repaired Inconel 718 with a non-uniform microstructure, Mater. Sci. Eng. A. 688 (2017) 480–487.

[15] Z. Li, B. He, Q. Guo, Strengthening and hardening mechanisms of additively manufactured stainless steels: The role of cell sizes, Scr. Mater. 177 (2020) 17–21.

[16] G.P. Dinda, A.K. Dasgupta, J. Mazumder, Laser aided direct metal deposition of Inconel 625 superalloy: Microstructural evolution and thermal stability, Mater. Sci. Eng. A. 509 (2009) 98–104.

[17] K. Chen, R. Huang, Y. Li, S. Lin, W. Zhu, N. Tamura, J. Li, Z.-W. Shan, E. Ma, Rafting-enabled recovery avoids recrystallization in 3D-printing-repaired single-crystal superalloys, Adv. Mater. (2020) 1907064.

[18] Y. Li, D. Qian, J. Xue, J. Wan, A. Zhang, N. Tamura, Z. Song, K. Chen, A synchrotron study of defect and strain inhomogeneity in laser-assisted three-dimensionally-printed Ni-based superalloy, Appl. Phys. Lett. 107 (2015) 181902.

[19] R. Hielscher, H. Schaeben, A novel pole figure inversion method: specification of the MTEX algorithm, J. Appl. Cryst. 41 (2008) 1024–1037.

[20] N. Tamura, XMAS: A Versatile Tool for Analyzing Synchrotron X-ray Microdiffraction Data, in: R. Barabash, G. Ice (Eds.), Strain Dislocation Gradients from Diffr. Spat. Local Struct. Defects, World Scientific, London, 2014: pp. 125–155.

[21] J. Kou, K. Chen, N. Tamura, A peak position comparison method for high-speed quantitative Laue microdiffraction data processing, Scr. Mater. 143 (2018) 49–53.

[22] G. Zhou, J. Kou, Y. Li, W. Zhu, K. Chen, N. Tamura, Quantitative Scanning Laue Diffraction Microscopy: Application to the Study of 3D Printed Nickel-Based Superalloys, Quantum Beam Sci. 2 (2018) 13.

[23] O. Muránsky, L. Balogh, M. Tran, C.J. Hamelin, J.S. Park, M.R. Daymond, On the measurement of dislocations and dislocation substructures using EBSD and HRSD techniques, Acta Mater. 175 (2019) 297–313.

[24] D.M. Norfleet, D.M. Dimiduk, S.J. Polasik, M.D. Uchic, M.J. Mills, Dislocation structures and their relationship to strength in deformed nickel microcrystals, Acta Mater. 56 (2008) 2988–3001.

[25] E. Chauvet, C. Tassin, J.J. Blandin, R. Dendievel, G. Martin, Producing Ni-base superalloys single crystal by selective electron beam melting, Scr. Mater. 152 (2018) 15–19.

[26] Y. Li, K. Chen, N. Tamura, Mechanism of heat affected zone cracking in Ni-based superalloy DZ125L fabricated by laser 3D printing technique, Mater. Des. 150 (2018) 171–181.

[27] H. Xiao, S. Li, X. Han, J. Mazumder, L. Song, Laves phase control of Inconel 718 alloy using quasi-continuous-wave laser additive manufacturing, Mater. Des. 122 (2017) 330–339.

[28] S. Kou, Welding metallurgy, New Jersey, USA. (2003) 431–446.

[29] M. Gäumann, C. Bezençon, P. Canalis, W. Kurz, Single-crystal laser deposition of superalloys: Processing-microstructure maps, Acta Mater. 49 (2001) 1051–1062.

[30] K.G. Prashanth, J. Eckert, Formation of metastable cellular microstructures in selective laser melted alloys, J. Alloys Compd. 707 (2017) 27–34.

[31] Y.-J. Liang, J. Li, A. Li, X.-T. Pang, H.-M. Wang, Solidification path of single-crystal nickel-base superalloys with minor carbon additions under laser rapid directional solidification conditions, Scr. Mater. 127 (2017) 58–62.

[32] K. Zhao, Y.H. Ma, L.H. Lou, Z.Q. Hu, μ Phase in a Nickel Base Directionally Solidified Alloy, Mater. Trans. 46 (2005) 54–58.

[33] G. Wang, J. Liang, Y. Zhou, L. Zhao, T. Jin, X. Sun, Variation of crystal orientation during epitaxial growth of dendrites by laser deposition, J. Mater. Sci. Technol. 34 (2018) 732–735.

[34] J.W. Aveson, P.A. Tennant, B.J. Foss, B.A. Shollock, H.J. Stone, N. D'Souza, On the origin of sliver defects in single crystal investment castings, Acta Mater. 61 (2013) 5162–5171.

[35] T. Tinga, W.A.M. Brekelmans, M.G.D. Geers, Cube slip and non-Schmid effects in single crystal Ni-base superalloys, Model. Simul. Mater. Sci. Eng. 18 (2010).

Figure 1. The cellular microstructures in the DEDed superalloy. OM images collected from the (a) longitudinal section and (b) cross sectional specimens. The yellow arrows in (a) and (b) denote the fusion lines. (c) An enlarged view of (b) showing the typical cell morphology. (d) BSE SEM image showing the dispersed precipitates along the cell boundaries from the cross-sectional view.

Figure 2. EDS element distributions collected from the cross-sectional specimen.

Figure 3. The phase distribution in the DEDed superalloy. The combination of (a) BSE SEM and (b) TEM dark field images reveals two types of γ' morphologies. SEAD patterns evidence (c) the coherent γ/γ' microstructure and (d) the μ-phase precipitates.

Figure 4. Crystal orientation and misorientation analysis of cross-sectional specimen. (a) IPF-Z and (b) KAM maps of an EBSD measurement. The black and blue lines in (a) and (b) delineate the GBs with misorientation angles larger than 15°, respectively. (c) IPF-Z, (d) misorientation angle and (e) KAM maps of the μXRD scan. (f) A linear profile of point-to-point misorientation along the horizontal arrow in (e).

Figure 5. STEM TEM analysis of dislocation configurations at the cellular scale. (a) A full view of a cell colony and dislocation configurations, (b) near the cell boundary, and (c) in the cell interior.

Figure 6. Schematic illustration of the microstructures from the sub-millimeter to nanometer scales in the cross-sectional view of DEDed Ni-based superalloy.

Table 1. Nominal compositions of the substrate and powders.

Composition (wt%)	C	Cr	Co	Mo	W	Al	Ti	Ta	Ni
DZ125L substrate	0.12	8.74	9.54	2.21	6.46	5.03	3.18	3.96	Balance
DD4 powders	0.004	8.97	7.26	1.94	6.91	3.94	4.22	3.73	Balance

Supplementary Material

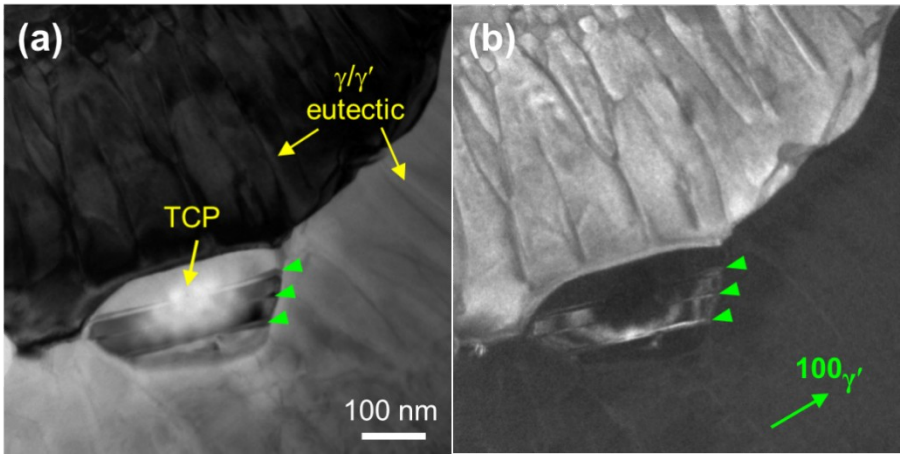

Figure S1. An enlarged view of lower-left corner of Fig. 3b clearly showing the lamellar structures of TCP phase. (a) Bright field image; (b) Dark field image illuminated by 100 reflection of ɣ′ precipitates. The green triangles denote the growth faults with lamellar morphology within the TCP particle.

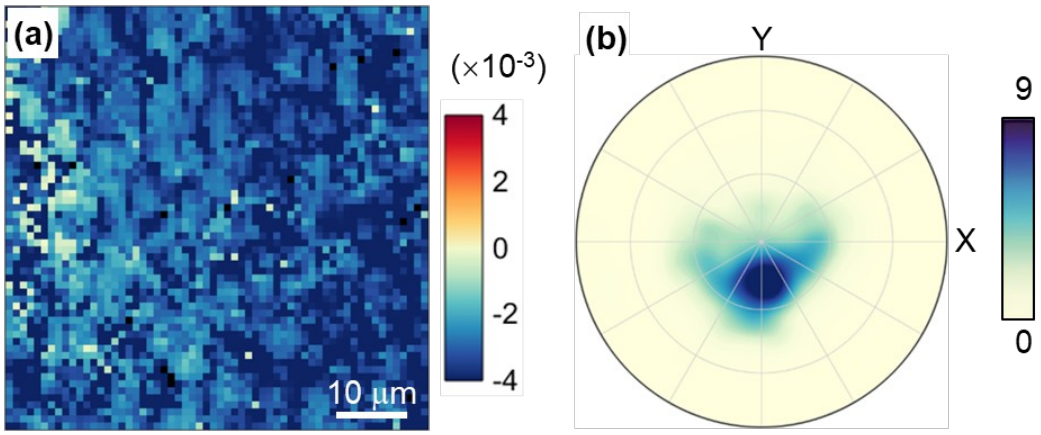

Figure S2. (a) The compressive principal strain map and (b) the corresponding stereographic projection of strain axes directions based on the strain tensors obtained by synchrotron X-ray microdiffraction technique.

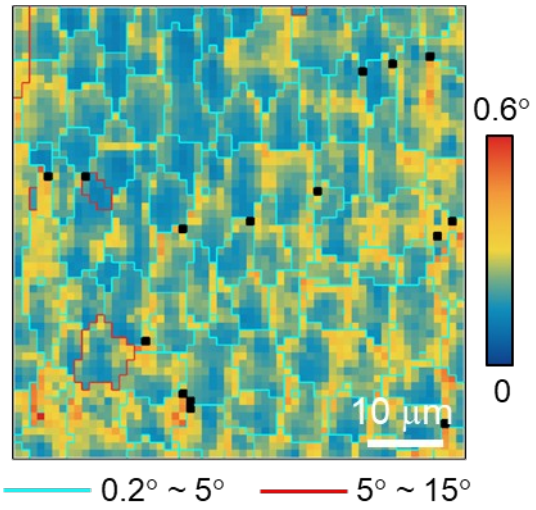

Figure S3. Average peak width map obtained from synchrotron X-ray microdiffraction data.